JACS
JOURNAL OF THE AMERICAN CHEMICAL SOCIETY
pubs.acs.org/JACS
Article

Origin of Scission Selectivity for Phosphoranyl Radicals in Photoredox Catalysis

Emily R. Wearing, Niharika Prakash Kaushik, Samuel T. Hugie, Matthew S. Sigman,* and Abigail G. Doyle*

Cite This: https://doi.org/10.1021/jacs.6c11233
Read Online
ACCESS | Metrics & More | Article Recommendations | Supporting Information

ABSTRACT: Phosphoranyl radicals are versatile synthetic intermediates that can form downstream radicals through α- and β-scission. However, the unclear origin of scission selectivity hinders the rational design of new transformations using these elementary steps. Here we report a comprehensive study of phosphoranyl radical scission mechanisms for sulfonamide nucleophiles. Using a combination of experimental, computational, and machine-learning-driven strategies, the primary factors influencing selectivity in these transformations were uncovered. Computational and experimental studies revealed an unexpected Curtin−Hammett scenario and demonstrated the impact of reaction stoichiometry on selectivity outcomes. Statistical modeling enabled selectivity prediction via an interpretable linear regression model, which revealed that small, electron-poor phosphines favor β-scission. Taken together, these studies expose the interplay of reaction conditions, phosphine properties, and alkene properties, which can be used to control selectivity in phosphoranyl-radical-mediated reactions of sulfonamides. These insights were harnessed to develop a photoredox-catalyzed phosphine-mediated hydrosulfonylation reaction of alkenes, the development of which makes primary sulfonamides the first example of a nucleophile with switchable scission selectivity controlled only by phosphine and reaction conditions for phosphoranyl-radical-mediated reactions.

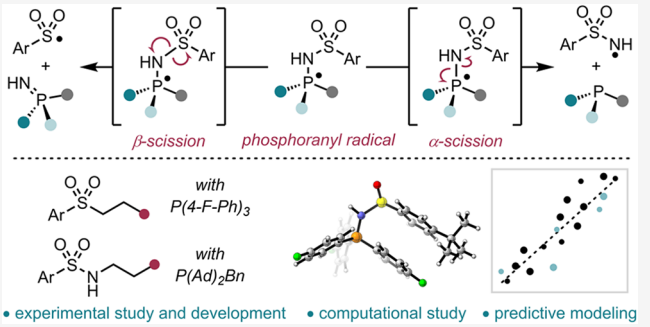

INTRODUCTION

Organic radicals are ubiquitous intermediates for diverse transformations. While radical chemistry has experienced a renaissance with the rise of photo-,[1−3] electro-,[4−7] and transition-metal catalysis,[8−11] limitations remain with respect to controlled generation and capture of radical species. Radical generation from unfunctionalized starting materials is particularly valuable, as this strategy provides direct entry into desired transformations from abundant compounds. One approach to generate radical intermediates from readily available nucleophilic functional groups is through fragmentation, or scission, of phosphoranyl radicals.[12−16] While phosphoranyl radicals are traditionally accessed through the addition of a radical intermediate to a phosphine,[12−16] photoredox catalysis has enabled the formation of these species under mild photochemical conditions from simple nucleophiles,[16−21] including alcohols,[22,23] carboxylic acids,[22,24,25] oximes,[26,27] sulfoxides,[28] and sulfonamides[29,30] (Figure 1A). This approach has been utilized in various synthetic transformations, including deoxygenation,[20−22,24,25,31,32] alkene hydrogenation,[33,34] and alkene hydroamination[29] or hydroazolation.[35,36]

While phosphoranyl-radical-mediated reactions have proven synthetic potential, there remains a general lack of understanding surrounding control of selectivity in these transformations, specifically regarding the scission processes through which organic radical intermediates are generated from the phosphoranyl radical (**3**) species (Figure 1A). In these photoredox-catalyzed reactions, P(III) phosphine **1** is oxidized to a phosphine radical cation (**2**), which is trapped through addition of a nucleophile to form P(IV) phosphoranyl radical **3**.[16,17] To form downstream radicals, intermediate **3** can fragment via α-scission, wherein the P−X bond undergoes homolytic cleavage to form a *X*-centered radical on the attacking nucleophile (**4**) and phosphine **1**, or β-scission, wherein the X−Y bond of the nucleophile homolytically cleaves to generate a *Y*-centered radical (**5**) and a P(V) byproduct (**6**) (Figure 1A).[16] The ability of phosphoranyl radicals (**3**) to fragment through either α- or β-scission provides the potential to develop tunable reactivity, wherein divergent transformations can be achieved from the same starting materials based on control of the reaction conditions. While this divergent reactivity would be highly

Received: June 1, 2026
Revised: August 1, 2026
Accepted: August 11, 2026

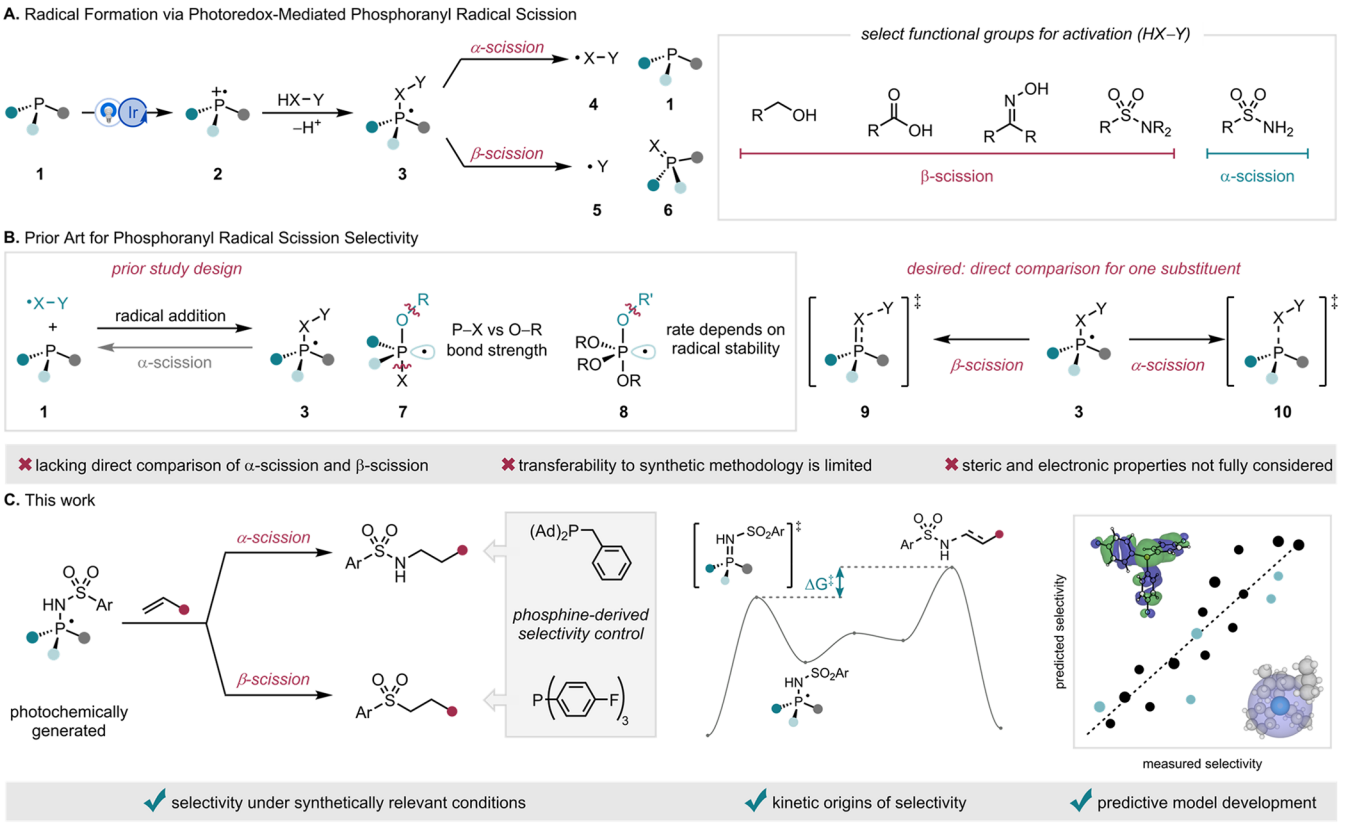

Figure 1. (A) Phosphoranyl radical formation and scission pathways in photoredox-catalyzed reactions, including selected nucleophiles reported for phosphoranyl-radical-mediated transformations. (B) Previous studies of scission selectivity and kinetics, and representative transition states for scission selectivity of the same nucleophilic phosphoranyl radical substituent. (C) This work: an experimental and data-driven study of phosphoranyl radical scission selectivity in photoredox-mediated reactions, including understanding and development of phosphine-driven selectivity control, kinetic origins of selectivity, and a predictive selectivity model.

desirable, there is no known phosphoranyl-radical-mediated method to activate the same nucleophile for different reaction outcomes based on the choice of phosphine reagent.

To rationally develop new transformations that achieve tunable selectivity through α- or β-scission, a comprehensive understanding of selectivity determination in phosphoranyl-radical-mediated reactions is required. Prior studies of scission selectivity have focused on phosphoranyl radicals generated through addition of a radical (i.e., X–Y, Figure 1B) to a P(III) center (**1**),[12−14,30] inherently limiting study of α-scission of the incoming group, as α-scission is the microscopic reverse of radical addition, making the origin of any product arising directly from the incoming radical unclear (Figure 1B). As such, early studies focused on comparing scission of two differing groups in a phosphoranyl radical intermediate (**3**): β-scission of the incoming radical (−O−R group in **7**), versus α-scission of one of the phosphine substituents (−X in **7**).[37−41] These studies, conducted through both EPR spectroscopy and analysis of phosphine products, demonstrated that relative bond strengths of the two groups involved in scission were the primary driver of selectivity.[12−14,37−41] This conclusion was later supported by work from Bietti and co-workers, who reported β-scission kinetics for a variety of alkoxy radicals reacting with trialkyl phosphites (via **8**), and determined that the rate of β-scission was influenced primarily by the stability of the resulting radical.[42] A recent study from Schmidt and co-workers similarly explored kinetics for sulfur atom transfer (SAT) to phosphines from thiyl radicals, a process involving β-scission, and found that the relative rate of SAT to the phosphine was influenced by phosphine identity, with phosphines with increased electron-donating inductive effects favoring faster rates of SAT.[43] While insights regarding the influence of bond strength on α-scission have been used to design a hydroalkylation reaction,[44] prior mechanistic studies primarily focus on reaction outcomes with respect to phosphine-based species, and as such are not generally transferable to selectivity in synthetic methods, where control over both of the scission processes for the incoming nucleophile (**9** vs **10**, Figure 1B) is desired and additional elementary steps leading to product formation could influence selectivity outcomes.

To enable the development of tunable selectivity for phosphoranyl-radical-mediated transformations, a comprehensive understanding of how phosphine structure influences selectivity under synthetic conditions is required. Given our groups' long-standing interest in using data science to understand and predict reaction outcomes,[45−47] we envisioned that a data-driven approach leveraging existing phosphine DFT feature data sets (*Kraken*)[48] and photoredox-mediated, synthetically relevant conditions would allow us to understand and predict scission selectivity as a function of phosphine structure, enabling rational design of scission-mediated reactions. Here we report a combination of experimental, computational, and machine-learning-driven studies that uncover key features controlling scission selectivity for sulfonamide-derived phosphoranyl radicals (Figure 1C). These insights, which encompass the impacts of phosphine structure, reaction conditions, and

https://doi.org/10.1021/jacs.6c11233
J. Am. Chem. Soc. XXXX, XXX, XXX−XXX

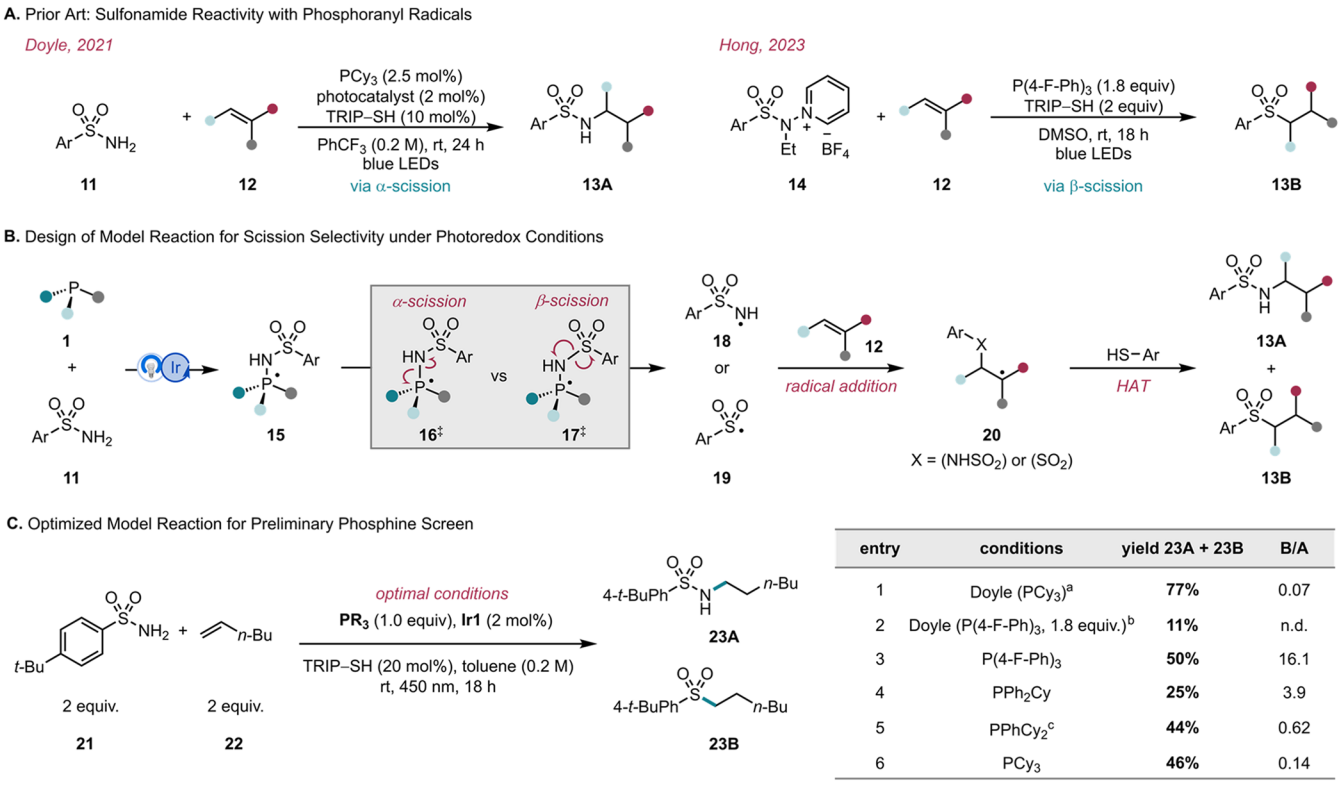

entry	conditions	yield 23A + 23B	B/A
1	Doyle (PCy_3)[a]	**77%**	0.07
2	Doyle ($P(4\text{-F-Ph})_3$, 1.8 equiv.)[b]	**11%**	n.d.
3	$P(4\text{-F-Ph})_3$	**50%**	16.1
4	PPh_2Cy	**25%**	3.9
5	$PPhCy_2$[c]	**44%**	0.62
6	PCy_3	**46%**	0.14

Figure 2. Identification and optimization of a model system. (A) Prior art for phosphoranyl radical activation of sulfonamide derivatives via α- and β-scission. (B) Design of a model system for studying scission selectivity. (C) Optimization of a model system and validation with varied phosphines. Table entries run under optimal conditions unless otherwise noted. [a] 5 mol % PCy_3, otherwise conducted under optimal Doyle conditions shown in (A); [b] with 1.8 equiv. $P(4\text{-F-Ph})_3$, otherwise conducted under optimal Doyle conditions shown in (A), n.d., not determined. Yield reported for **23B** only. [c] 10 mol % TRIP–SH, 23–24 h. **Ir1**, $[Ir(dFMeppy)_2(dtbbpy)]PF_6$; TRIP–SH, 2,4,6-triisopropylbenzenethiol.

alkene identity, provide a new understanding of scission selectivity, which we expect will enable the development of new and/or improved reactions that leverage phosphoranyl radical scission processes.

RESULTS AND DISCUSSION

Selection and Optimization of a Model System

We sought to develop a model system that could read out scission selectivity with a measurable reaction outcome, such as the ratio of α-scission product (product **A**) and β-scission product (product **B**), while being synthetically tractable and suitable for collecting a data set of approximately 50 data points to enable predictive modeling.

As a starting point, we examined phosphoranyl-radical-mediated reactions of sulfonamide derivatives with varied selectivity outcomes. Previous work from the Doyle group demonstrated that primary sulfonamides (**11**) can undergo hydroamination reactions of alkenes (**12**) to form anti-Markovnikov products (**13A**) via α-scission of phosphoranyl radical intermediates derived from catalytic PCy_3 (Figure 2A).[29] Phosphoranyl radicals derived from *N*-amidopyridinium salts of secondary sulfonamides (**14**) have also been shown by Hong and co-workers to undergo β-scission, enabling a variety of transformations including alkene hydrosulfonylation (**13B**).[30] Studies of selectivity for a related alkene difunctionalized reaction found that electron-poor triaryl phosphines with smaller cone angles led to higher yields, attributed to increased radical delocalization in the β-scission transition state.[30] However, since the mechanism of this reaction proceeds through the addition of an *N*-centered radical (NCR) arising from the fragmentation of the N–N bond of **14** to the phosphine (analogous to the prior study design shown in Figure 1B), it is unclear if any NCR-derived products arise from α-scission, precluding conclusions about the influence of the phosphine on both α- and β-scission processes.

Based on these prior studies, we envisioned a model reaction wherein a phosphoranyl radical **15** would be generated from **1** and **11** under photoredox conditions without requiring a radical precursor that could interfere with reaction selectivity outcomes (Figure 2B). Phosphoranyl radical **15** would then fragment via α- (**16**) or β-scission (**17**), generating *N*-centered radical (NCR) **18** or *S*-centered radical (SCR) **19**, respectively. From this point, the addition of either radical to alkene **12** would form intermediate **20**, ultimately providing hydroamination product **13A** (product **A**) or hydrosulfonylation product **13B** (product **B**) following hydrogen atom transfer (HAT). Assuming the two radicals arising from scission, **18** and **19**, are captured for the formation of their respective products, we hypothesized that the ratio of reaction products **B**:**A** (**13B**:**13A**) could be used to estimate scission selectivity (**17**:**16**).

While the proposed mechanism for the formation of **13A** is precedented in the Doyle hydroamination methodology,[29] the formation of **13B** via the proposed pathway has not been previously reported. As such, we sought to determine if β-scission reactivity for the formation of **13B** was possible under photoredox-mediated conditions. Performing the desired reaction of aryl sulfonamide **21** and 1-hexene (**22**) under modified hydroamination conditions (Figure 2C, entry 1) afforded a high yield of **23A**, and a small amount of **23B** (~5%

https://doi.org/10.1021/jacs.6c11233
J. Am. Chem. Soc. XXXX, XXX, XXX–XXX

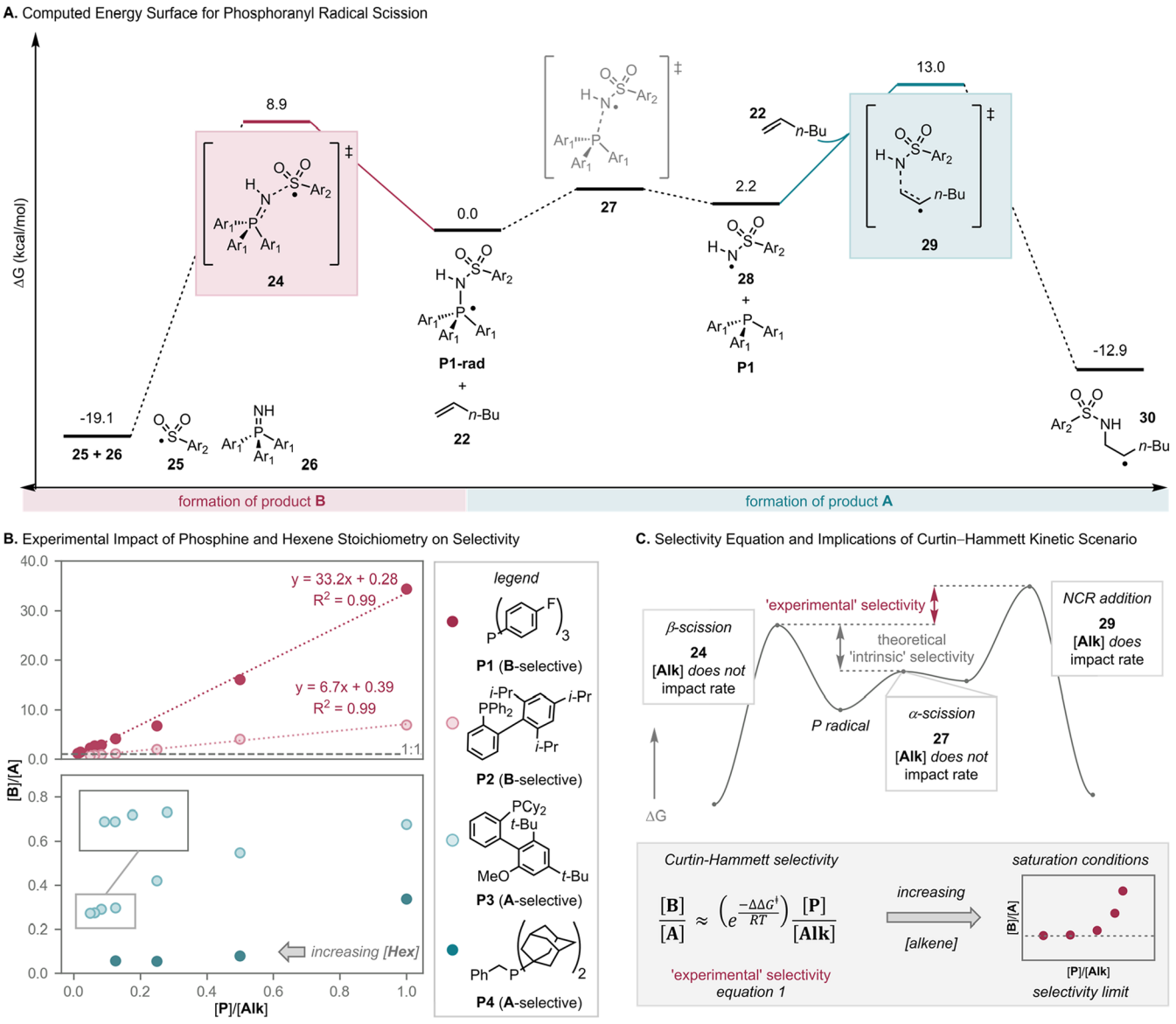

Figure 3. Computational and experimental mechanistic studies of the model system. (A) DFT-computed free energy surface ((U)ωB97X-D/def2-TZVP (SMD, toluene)//(U)ωB97X-D/def2-SVP). Ar_1 = 4-F-Ph; Ar_2 = 4-*t*-Bu-Ph. Radicals in transition state structures shown in their ultimate position for clarity. (B) Experimental comparison of **B**:**A** selectivity over a range of hexene concentrations. For this plot [**B**]/[**A**] represents **23B**/**23A**, [**Alk**] represents the hexene concentration. (C) Kinetic selectivity relationship under experimental and saturation conditions.

yield), indicating both α-scission and β-scission of primary sulfonamides is possible in the same pot. Seeking to optimize formation of **23B**, we identified a triaryl phosphine P(4-F-Ph)$_3$ with precedent for β-scission reactivity,[30] and found that when used in excess (1.8 equiv), this phosphine led to an increased 11% yield of **23B** under photoredox conditions (entry 2). To balance the requirements of β-scission, which is stoichiometric in phosphine, and α-scission, which has been reported to perform less well under higher phosphine loadings,[29] we elected to use phosphine as the limiting reagent, which, after optimization, ultimately raised the yield of **23B** to 47% while still allowing formation of measurable **23A** (**B**/**A** = 16.1, entry 3) (see Supporting Information for optimization details). To validate this model system for the study of scission selectivity with respect to phosphine identity, we performed the reaction with a few phosphines spanning from triaryl phosphine P(4-F-Ph)$_3$ (entry 3) to trialkyl (PCy_3, entry 6), and found that the **B**:**A** ratio varied, indicating selectivity is controlled by phosphine identity. Furthermore, moderate yields of **23A** (40%) were still accessible with PCy_3 under our optimized conditions, highlighting the successful balance of conditions favoring α- and β-scission processes.

Mechanistic Studies of the Model System

With our model system in hand, we sought to understand how the experimentally observed **B**:**A** selectivity related to the reaction energy profile of β- and α-scission. We began our investigations with density functional theory (DFT) calculations of the free energy surface for P(4-F-Ph)$_3$ (**P1**), a **B**-selective phosphine from our preliminary screen. Starting from the phosphoranyl radical (**P1-rad**), we computed transition states and related intermediates for β-scission (**24**), *S*-centered radical (SCR) (**25**) addition to hexene (**22**) (not shown), and *N*-centered radical (NCR) (**28**) addition to hexene (transition state **29**) (Figure 3A). While the transition state structure for α-scission (**27**) could not be located, we expect that this transition

https://doi.org/10.1021/jacs.6c11233
J. Am. Chem. Soc. XXXX, XXX, XXX−XXX

state is kinetically favorable.[12−14,29,30] Interestingly, we find that while β-scission (**24**) is an irreversible selectivity determining transition state for the formation of product **23B**, based on an assumed low barrier for α-scission, the selectivity-determining step for the formation of **23A** is addition of the NCR (**28**) to hexene (transition state **29**) (see SI for further discussion of selectivity- versus rate-determining steps in this system). While the computed energy surface qualitatively aligns with our experimental results, the computed difference in energy ($\Delta\Delta G^{\ddagger}$) between **24** and **29** is slightly higher than we would expect based on the measured **B**:**A** selectivity (see SI for details). Additionally, an energy surface computed for an **A**-selective phosphine, PAd_2Bn (**P4**), showed the same kinetic relationship between the transition states (see SI section 4.2.2). These results suggest that selectivity is controlled not by a simple competition between α- and β-scission ("intrinsic" selectivity), but by a Curtin−Hammett-like[49−51] scenario wherein an α-scission equilibrium between **P1-rad** and **P1** + **28** results in selectivity determination through a competition between β-scission (**24**) and NCR-addition (**29**), as described by eq 1. Importantly, the Curtin−Hammett scenario controlling this reaction involves competition between two differing elementary steps, meaning selectivity is influenced by the relative concentrations of phosphine (**P**) and alkene (**Alk**) as well as the $\Delta\Delta G^{\ddagger}$ between the rate-determining steps.

$$\frac{[\mathbf{B}]}{[\mathbf{A}]} \approx \frac{\frac{d[\mathbf{B}]}{dt}}{\frac{d[\mathbf{A}]}{dt}} = (e^{-\Delta\Delta G^{\ddagger}/RT})\frac{[\mathbf{P}]}{[\mathbf{Alk}]} \quad (1)$$

To experimentally validate this kinetic scenario, we tested varied [**P**]:[**Alk**] ratios in the model reaction with a set of phosphines with differing selectivity (**P1**−**P4**) (Figure 3B). Based on eq 1, increasing alkene concentration ([**Alk**]) would decrease the phosphine to alkene ratio, leading to a shift in selectivity toward product **A**. The relationship between **B**:**A** and [**P**]:[**Alk**] should be linear, with a slope dependent on $\Delta\Delta G^{\ddagger}$ of the selectivity-determining steps. As anticipated, increasing the concentration of hexene in our model reaction leads to decreased β-scission selectivity for all phosphines, supporting the existence of a low-energy α-scission transition state and the proposed Curtin−Hammett scenario (Figure 3B). Interestingly, while the two **B**-selective phosphines (**P1**, **P2**) display a good linear relationship, the two **A**-selective phosphines (**P3**, **P4**) exhibit saturation behavior at increased hexene concentrations, with the concentration of hexene required to reach saturation being phosphine-dependent. The initiation of saturation behavior can also be observed at high equivalents of hexene for the moderately **B**-selective phosphine **P2**. Notably, at these high hexene concentrations, this phosphine (**P2**) exhibits slight selectivity for product **23A**, despite being initially **B**-selective.

These results reveal an unexpected selectivity scenario with synthetic implications. Rather than arising from direct competition between α- and β-scission ("intrinsic" selectivity), selectivity arises from a Curtin−Hammett-like scenario. Experimental results are consistent with this kinetic relationship, with a linear relationship between [**P**]:[**Alk**] and selectivity (**B**:**A**) at synthetically relevant concentrations of hexene. As the Curtin−Hammett regime is operative under these conditions, we consider this as the "experimental" selectivity, determined by the $\Delta\Delta G^{\ddagger}$ of **24** and **29** and reaction stoichiometry (eq 1) (Figure 3C). However, at increased alkene concentrations, we observe a breakdown of this linear Curtin−Hammett relationship and the appearance of saturation behavior. As alkene equivalents increase, the rate of NCR-addition (**29**) increases to become closer to the rate of α-scission (**27**), violating the pre-equilibrium assumption of the Curtin−Hammett scenario, and causing selectivity determination to deviate from the derived eq 1. Given the observation that the onset of saturation is impacted by both phosphine identity and alkene identity (See SI Section 2.3), saturation represents a move toward an "intrinsic" selectivity regime but does not represent a direct competition between the two scission steps. Rather, the onset of saturation behavior is likely related to rates of α-scission and NCR-addition, and possibly by the reaction to form **23A** approaching diffusion-limited rates. Interestingly, the saturation-dependent selectivity limit is generally reached with moderate to high **A**-selectivity, though this value is phosphine-dependent.

Comparing phosphines **P1**−**P4** under this lens, we can assess selectivity under the "experimental" selectivity regime as a function of the transition state barrier for β-scission (**24**), rather than as a competition of β-scission and α-scission. Since phosphine identity should not influence the NCR-addition transition state barrier, changes in selectivity between phosphines will be driven by changes in β-scission transition state energy. With respect to the saturation-dependent selectivity limit, these studies reveal that **A**-selective phosphines generally reach saturation with lower **B**/**A** values than **B**-selective phosphines, despite saturation generally occurring in an **A**-selective regime. Furthermore, phosphines that are **B**-selective under experimental conditions have lower selectivity for product **A** as they approach saturation, with highly **A**-selective phosphine **P4** reaching saturation at a **B**:**A** ratio of ∼0.05:1.0, moderately **A**-selective phosphine **P3** reaching saturation at a **B**:**A** ratio of ∼0.3:1.0, and **B**-selective phosphine **P2** beginning to approach saturation at a **B**:**A** ratio of ∼0.8:1.0. These data indicate that while "experimental" selectivity differs considerably from selectivity under saturation conditions, these values seem to be related with respect to the relative selectivity within the phosphine series.

Taken together, these studies provide essential insight into the origin of phosphoranyl radical scission selectivity under synthetic conditions. Rather than being controlled by direct competition between β-scission and α-scission, the ratio of products **B** and **A** is determined through a complex interplay of transition state barriers and reaction stoichiometry. Importantly, for all cases where saturation is reached, the saturation-dependent selectivity limit favors α-scission and product **A**, indicating that β-scission (**B**) selective reactions require a balance of low-energy β-scission transition states and slower NCR-addition.

Factors Influencing Reaction Selectivity

Based on the above, **B**:**A** selectivity in these phosphoranyl-radical-mediated reactions is influenced by three major factors:

1. *Reaction stoichiometry*: Specifically, the ratio of phosphine and alkene in the reaction, where increasing the concentration of the alkene relative to the phosphine shifts selectivity toward α-scission product **A**.
2. *Phosphine identity*: Wherein modulation of the β-scission transition state based on phosphine structure is expected to control scission selectivity.
3. *Alkene identity*: The identity of the alkene will influence selectivity via changes in the energy of the NCR-addition transition state.

https://doi.org/10.1021/jacs.6c11233
J. Am. Chem. Soc. XXXX, XXX, XXX−XXX

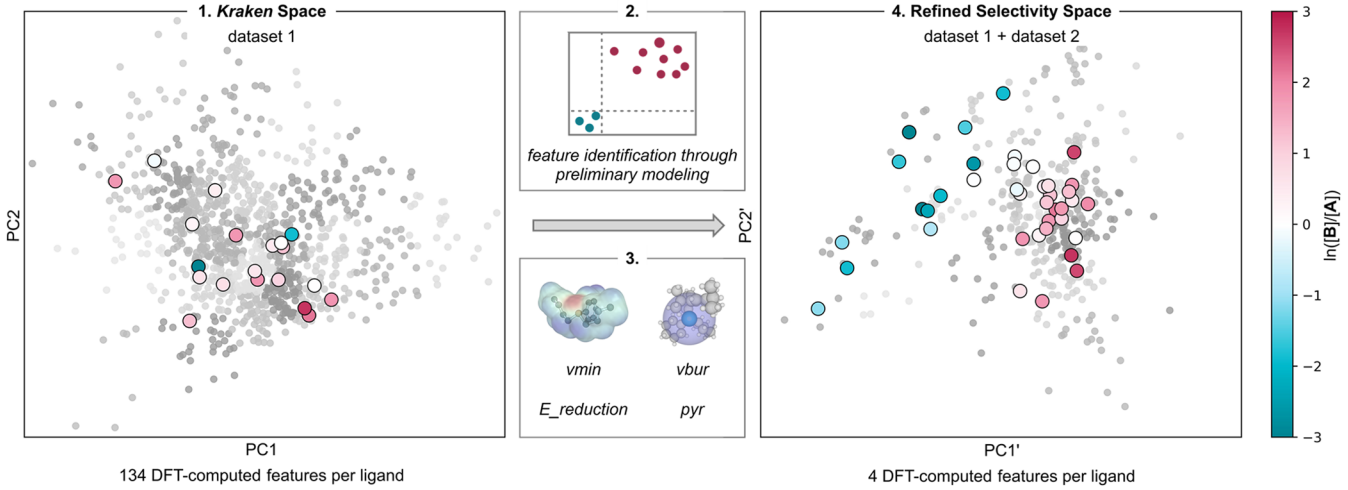

Figure 4. Workflow for data set selection from phosphine chemical space. Step 1. Experimental results from the first data set on *Kraken* chemical space (left). Steps 2 and 3. Preliminary modeling and feature selection. Step 4. Experimental results from both data sets on refined selectivity 4-feature chemical space. Definitions: vmin, minimum of the electrostatic potential at P (Boltzmann average); nbo_bds, average P−C antibonding orbital energy (Boltzmann average); vbur, buried volume (radius 3.5 Å, Boltzmann average); E_reduction, ionization potential (Boltzmann average); and pyr, minimum value of pyramidalization.

While eq 1 provides the relationship between reaction conditions and selectivity, the impact of the phosphine structure and alkene identity remained unknown.

Modeling Selectivity as a Function of Phosphine Structure

Given the challenges encountered using DFT to computationally study these systems (see SI section 4 for details), we hypothesized that a machine-learning-driven approach would be well-suited to study phosphine structure−selectivity relationships. Through the generation of predictive models, machine learning can uncover underlying trends in a data set with respect to phosphine structure and selectivity, facilitating *in silico* screening of phosphine candidates for future applications.

To train predictive models, we envisioned collecting selectivity data using a representative data set of monophosphines. This data would then be modeled as a function of phosphine structural features extracted from the *Kraken* phosphine database, which contains DFT-level stereoelectronic properties of >1600 monophosphines.[48] Based on the "experimental" selectivity regime, the rate of β-scission will change with phosphine identity while the rate of NCR-addition remains constant, resulting in a data set representative of the relationship between phosphine structure and β-scission transition state energy.

To select a data set of phosphines covering the breadth of chemical space, we employed a dimensionality reduction and clustering approach, wherein the *Kraken* PC_3-type phosphine space was grouped based on similarity.[48] We utilized all DFT-computed features in *Kraken* to conduct principal component analysis (PCA) and clustering of the points with a *k*-nearest neighbors (*k*-NN) algorithm (Figure 4). Points near the center of each cluster were selected to ensure a data set representative of chemical space.[48,52] We selected 24 phosphines as an initial data set, and found that in the model reaction, 20/24 gave measurable **B**:**A** selectivity. The majority of these 20 phosphines were selective for product **B**, leaving only 3 **A**-selective phosphines. To train effective machine learning models, a more well-distributed data set was required. However, examination of the reaction outcomes in the *Kraken* chemical space revealed that **A**-selective phosphines were not located in the same vicinity, making identification of additional **A**-selective phosphines difficult (Figure 4, step 1). To overcome this challenge, we used a "chemist-in-the-loop" active learning strategy,[53] wherein the initial 24-point data set was analyzed using a combination of data science approaches (step 2) to identify features most important to selectivity outcomes (step 3). These features were then used to generate an alternative chemical space map defined by only four of the *Kraken* features (Figure 4, step 4). By limiting the features to only those identified to be related to selectivity, the refined selectivity space is better divided with respect to selectivity outcomes. As such, the **A**-selective phosphines from the first data set were located in the same region, allowing oversampling of the nearby clusters where phosphines were expected to provide **A**-selectivity. Collecting additional data for this second round of phosphine selections resulted in a more balanced selectivity distribution (~40% **A**-selective phosphines), providing a data set representative of both phosphine chemical space and reactivity space (Figure 4, right plot). Collecting data for 7 additional phosphines for model validation completed our selectivity data set (total 46 phosphines, ~40% **A**-selective).

Using experimental **B**:**A** ratios from our data set (as ln(**B**/**A**)) and phosphine features from the *Kraken* database, we trained models for classification and regression tasks and found that a 4-feature linear regression model was the highest performing for prediction (train MAE = 0.437, R^2 = 0.889; validation MAE = 0.429, R^2 = 0.930; external test MAE = 0.802, R^2 = 0.633) (Figure 5A). The features in the final model describe a combination of stereo- and electronic phosphine properties, with the phosphine HOMO energy (fmo_e_homo) and P−C antibonding orbital energy (nbo_bds) representing electronic features, pyramidalization (pyr) representing a stereoelectronic feature, and buried volume (%vbur) representing a steric feature. These features were also observed in highly ranked models throughout our modeling efforts, providing additional confidence that they represent true structure−selectivity relationships. The successful use of *Kraken* features of the parent phosphine demonstrates the utility of the *Kraken* database for predictive modeling and provides the opportunity to use this model for prediction on all PC_3-phosphines in the *Kraken* data

https://doi.org/10.1021/jacs.6c11233
J. Am. Chem. Soc. XXXX, XXX, XXX−XXX

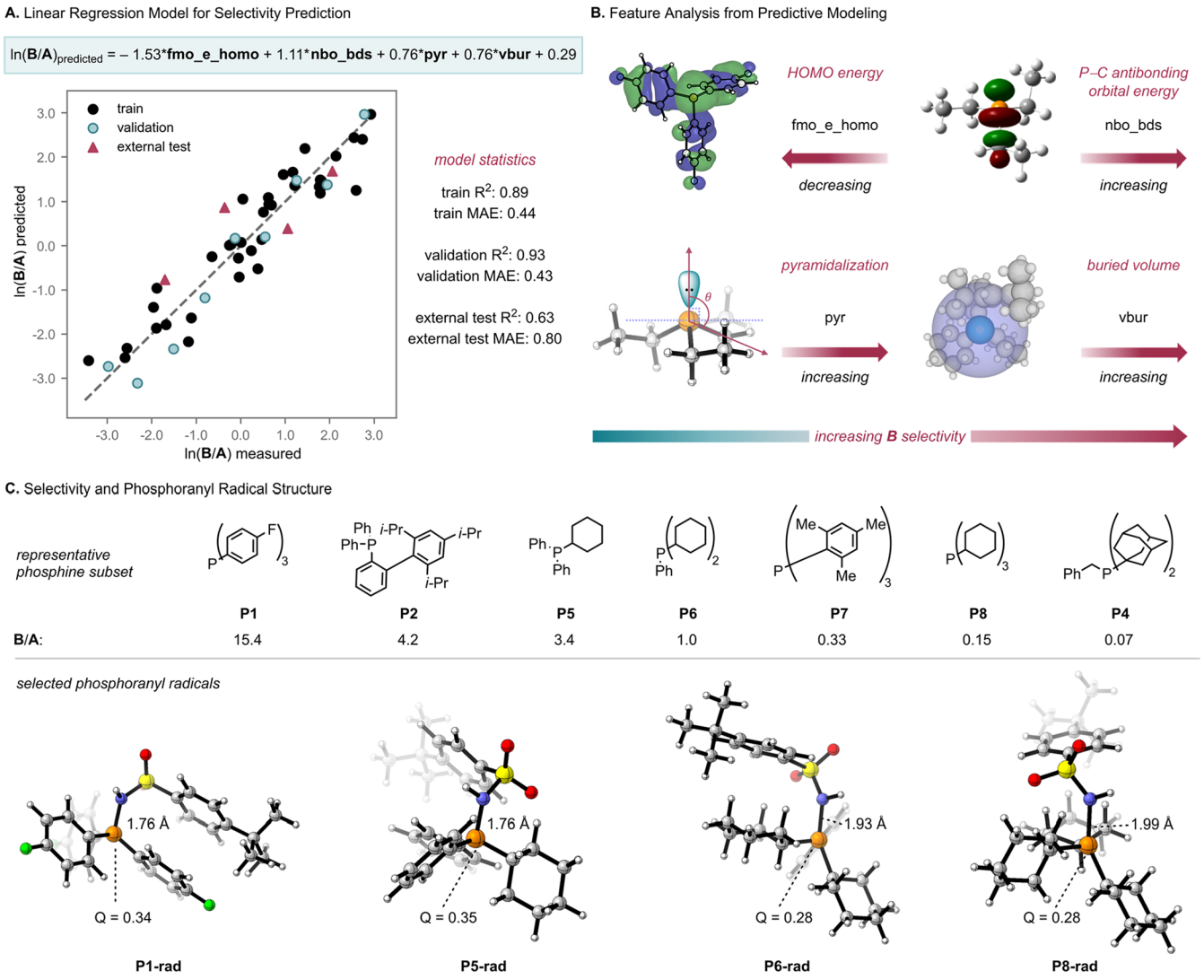

Figure 5. (A) 4-Feature linear regression model for ln(**B**/**A**) prediction. **B**/**A** represents **23B**/**23A**. (B) Feature interpretation showing trends with increasing **B**-selectivity. (C) DFT study of a phosphoranyl radical subset and relation of phosphoranyl radical features to selectivity. Phosphoranyl radical structures derived from model sulfonamide 4-*tert*-butylbenzenesulfonamide and the relevant phosphine. DFT: ((U)ωB97X-D/def2-TZVP (SMD, toluene)//(U)ωB97X-D/def2-SVP). *Definitions:* fmo_e_homo, energy of the HOMO (Boltzmann average); nbo_bds, average P−C antibonding orbital energy (Boltzmann average); pyr, minimum value of pyramidalization; vbur, buried volume (radius 3.5 Å, Boltzmann average); and MAE, mean absolute error.

set without any additional calculations, enabling future applications.

Given the interpretability of linear regression models and the chemically meaningful features in the *Kraken* database, we hypothesized that the features included in the predictive MLR model could also be used to understand structure−selectivity relationships, despite not representing transition state or phosphoranyl radical intermediate structures. Prior to feature interpretation, we analyzed the collinearity among the four descriptors in the MLR model and found that although none of the features were strongly correlated, there was a moderate correlation between pyramidalization (pyr) and buried volume (vbur) ($R^2 = 0.52$), arising due to their shared sensitivity to steric environments. Analyzing each feature, we find that the **B**:**A** ratio increases as HOMO energy decreases, and as P−C antibonding orbital energy and pyramidalization increase (Figure 5B). Based on the collinearity analysis, we hypothesize that pyramidalization is capturing the dominant stereoelectronic trend associated with phosphine geometry, including steric influences, while buried volume provides additional resolution for phosphines where pyramidalization is similar despite steric differences (see SI section 3.2.2). Furthermore, energy decomposition analysis indicates that the buried volume feature correlates with dispersion energy, suggesting that it may serve as a proxy for capturing noncovalent interactions that aid in the stabilization of the phosphoranyl radical intermediates. Thus, the buried volume feature may be functioning as more of a context-dependent term in the model than an independent monotonic descriptor of selectivity. Overall, our analysis suggests that more

https://doi.org/10.1021/jacs.6c11233
J. Am. Chem. Soc. XXXX, XXX, XXX−XXX

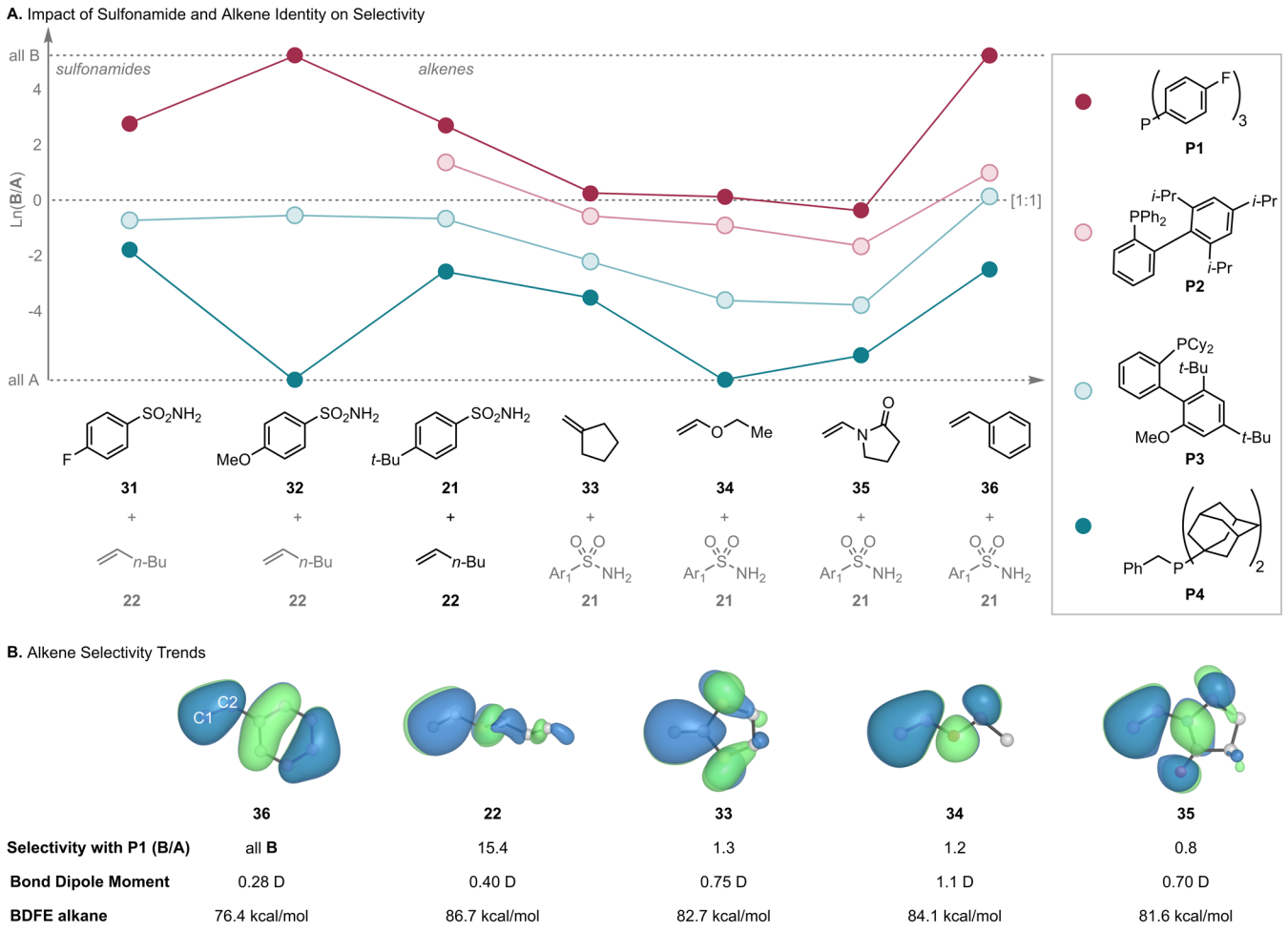

Figure 6. (A) Relationship of sulfonamide and alkene identity and selectivity outcomes. Ar_1 = 4-*tert*-butylbenzene. (B) Computed features of the alkenes used in this study. DFT features computed using BDFE, (U)ωB97X-D/def2-TZVP//(U)ωB97X-D/def2-SVP; Hirshfeld charge, (U)ωB97X-D/def2-SVP. BDFE, bond dissociation free energy.

electron-poor and pyramidalized phosphines favor β-scission and product **23B**.

While the *Kraken* structural features cannot be directly related to the phosphoranyl radical or transition state structure, we expect that these general properties transfer from the parent phosphine structures in *Kraken* to represent phosphoranyl radicals that can better stabilize the β-scission transition state, leading to higher **B**-selectivity overall. To examine this relationship, we used DFT to compute optimized β-scission transition states for a set of 7 phosphines (**P1**, **P2**, **P4**−**P8**) and extracted a set of atomic and geometric features (i.e., atomic charge, spin density, bond length) (Figure 5C). These transition state features, along with phosphoranyl radical features for each selected phosphine, were used to assess how the structures of these intermediates relate to selectivity and to the properties identified from the *Kraken* features.

Overall, phosphoranyl radical features provided the strongest correlations with selectivity (ln(**B**/**A**)). Of these features, the length of the P−N bond in the phosphoranyl radical has the strongest correlation to **B**:**A** selectivity, where phosphoranyl radicals with short P−N bonds favor **B**-selectivity. This feature could be represented in the linear regression model by both steric and electronic *Kraken* features, as the P−N bond length is influenced by the favored phosphoranyl radical geometry, which is controlled by a variety of factors. For this limited phosphine subset, it was found that the **B**-selective phosphines have accessible and low-energy tetrahedral geometries (**P1, P2, P5**), compared to unselective (**P6**) and **A**-selective phosphines (**P4**, **P7**, **P8**), for which only trigonal bipyramidal (TBP) structures were located computationally (Figure 5C). These differences in geometry are consistent with the correlated phosphoranyl radical features, particularly P−N bond length, with TBP phosphoranyl radicals generally having longer P−N bonds than tetrahedral phosphoranyl radicals.

Selectivity (ln(**B**/**A**)) is also correlated with the charge on the *P*-atom, aligned with the inclusion of the *Kraken* fmo_e_homo feature in the linear regression model, and indicating that phosphoranyl radicals with more electron-poor phosphine atoms favor formation of product **B**. Additionally, the spin on the *P*-atom in the phosphoranyl radical is moderately correlated to **B**-selectivity (Spearman ranked correlation = −0.64), with phosphoranyl radicals that have greater delocalization of the unpaired spin having greater selectivity for product **B**. This result is consistent with the conclusions of Hong and co-workers,[30] demonstrating the ability of our approach to identify important features describing selectivity for both known and previously unknown features influencing selectivity control in these complex systems.

Based on the above correlations, we conclude that more electron-poor phosphoranyl radicals and phosphoranyl radicals

https://doi.org/10.1021/jacs.6c11233
J. Am. Chem. Soc. XXXX, XXX, XXX−XXX

with shorter P−N bonds favor **B**-selectivity through the formation of more stabilized β-scission transition states. As the β-scission transition states tend to have shorter P−N bonds and a more tetrahedral-like structure than the parent phosphoranyl radicals, phosphoranyl radicals that can stabilize these types of geometries can be expected to result in more facile β-scission. While the relationships between phosphoranyl radical structure and features and the *Kraken* features used for modeling cannot be comprehensively characterized with our small data set, this analysis reveals key connections between each feature set, and that structural information from both the *Kraken* phosphines and the phosphoranyl radicals can provide handles for understanding and controlling **B**:**A** selectivity.

Impact of Alkene and Sulfonamide Identity on Reactivity

Having determined how phosphine structure controls selectivity, we turned to exploring the impact of alkene and sulfonamide identity on the **B**:**A** ratio. While the sulfonamide starting material is involved in both selectivity-determining steps, the alkene was expected to exclusively impact the rate of NCR-addition (**29**, Figure 3A). Preliminary computational assessment of the model reaction with various alkenes and aryl-substituted sulfonamides revealed that changes in sulfonamide identity had minimal impact on $\Delta\Delta G^{\ddagger}$, while changes in alkene identity changed the magnitude of $\Delta\Delta G^{\ddagger}$ substantially (see SI for details). Based on these computational studies, we hypothesized that changing the alkene identity would impact the magnitude of the **B**:**A** selectivity for a specific phosphine, but that overall, the relative order of selectivity among phosphines would remain the same.

On the basis of our preliminary calculations, we selected 5 alkenes and 3 sulfonamides with which to measure experimental selectivity for a subset of phosphines selected to represent the larger data set (Figure 6A). The identity of the aryl-substituted sulfonamide had a small impact on selectivity for two of the sulfonamides tested (**21, 31**), while sulfonamide **32** showed a slight difference in selectivity profile, with phosphines **P1** and **P4** showing complete selectivity for product **B** and product **A**, respectively. Though product yields were low for sulfonamide **32**, this interesting example represents a complete switch in selectivity based solely on the phosphine identity. Notably, our model reaction was found to be limited in scope to aryl-substituted sulfonamides, precluding a comparison of more diverse sulfonamides that may be expected to have a larger impact on selectivity.

As anticipated, the alkene identity has a significant impact on selectivity, with many alkenes (**33**−**35**) shifting the reaction toward **A**-selectivity. Specifically, for 1,1-disubstituted alkene **33** and vinyl ether **34**, even the most **B**-selective phosphine **P1** achieves only very modest selectivity toward product **B** (**B**/**A** = 1.3 or 1.2, respectively, for phosphine **P1**). For the vinyl pyrrolidine substrate **35**, no phosphine favored product **B**, with the most **B**-selective phosphine **P1** having a modest favorability toward product **A** (**B**/**A** = 0.8). For styrene (**36**), the selectivity values were more comparable to those of hexene, although phosphine **P3**, which is generally moderately **A**-selective, slightly favored product **B** (**B**/**A** = 1.2).[54] Crucially, in all cases, the relative selectivity ranking for the four phosphines remains the same, indicating that while alkene identity is an important factor in determining selectivity, the selectivity rankings provided by the MLR model are still suitable for predicting relative phosphine selectivity for substrates beyond sulfonamide **21** and hexene **22**.

Initial assessment of the five alkenes used for this study reveals that electron-rich alkenes shift selectivity toward **A**-selective reaction outcomes (**33**−**35**). To provide a more quantitative assessment of the alkenes, we extracted features related to the alkene carbon atoms (C1, terminal carbon; C2, internal carbon) from DFT-optimized alkene structures (Figure 6B). We found that the features that best categorize the five alkenes with respect to selectivity are the molecular dipole moment and the bond dipole moment for the C1═C2 bond, with the more **B**-selective alkenes **22** and **36** having a lower bond dipole moment than more **A**-selective alkenes **33**−**35**. For the more polarized alkenes, we conclude that the selectivity-determining step for the formation of product **A**, NCR-addition, is favored due to the increased polarization and electron density on the terminal carbon (C1) of the alkene. Visual assessment of the HOMO orbitals of these alkenes (Figure 6B) also demonstrates that for the nonaryl-containing alkenes, the more **A**-selective alkenes **33**−**35** have less symmetry in their π-orbitals than **B**-selective alkene **22**.

We also expected that the generation of a more stabilized radical (relative to that for hexene) during NCR-addition could lead to an increase in **A**-selectivity through analogous stabilization of the partial spin in the NCR-addition transition state. To probe this, we computed the bond dissociation free energy (BDFE) for a C−H bond on C2 of an alkane model system corresponding to each alkene substrate. As the radical corresponding to the dissociation of the specified C−H bond is in the same position as the radical in the post NCR-addition intermediate (**30**), we used the computed BDFE values as an estimate of stabilization of this species, which we expect to correspond to potential stabilization of the NCR-addition transition state (**29**). For the aliphatic alkenes (**22**, **33**−**35**), more **B**-selective alkenes correspond to lower BDFE values in their respective alkanes. While ethylbenzene (representing styrene **36**) has the lowest BDFE, it generally has higher selectivity for product **B**, similar to hexene. Given potential differences between aliphatic and conjugated alkenes, we cannot rule out that radical stability has an influence on selectivity, along with bond polarization in these systems.

Control of Scission Selectivity

With our new understanding of the impact of phosphine structure and alkene identity on selectivity, the framework for selectivity control in these phosphoranyl-radical-mediated transformations allows for general guidelines to be discussed:

1. *Reaction stoichiometry*: Selectivity is influenced by the ratio of phosphine and alkene in the reaction, where increasing the ratio of [**P**]/[**Alk**] increases the **B**/**A** ratio.
2. *Phosphine identity*: Phosphine identity has a strong influence over selectivity, with electron-poor, pyramidalized phosphines favoring the formation of product **B** and higher **B**:**A** ratios. While the overall selectivity depends on a variety of factors, our studies indicate that the selectivity ranking for phosphines remains the same across a series of alkenes and reaction conditions. Predicted selectivity rankings of *Kraken* phosphines[48] are available as part of an interactive Jupyter notebook included with the Supporting Information for this work.
3. *Alkene identity*: For a given phosphine, alkene identity can influence selectivity outcomes, with more polarized alkenes providing greater selectivity for product **A** and lower **B**/**A** ratios. Overall, alkenes for which *N*-centered radical addition is more favored should be expected to

https://doi.org/10.1021/jacs.6c11233
J. Am. Chem. Soc. XXXX, XXX, XXX−XXX

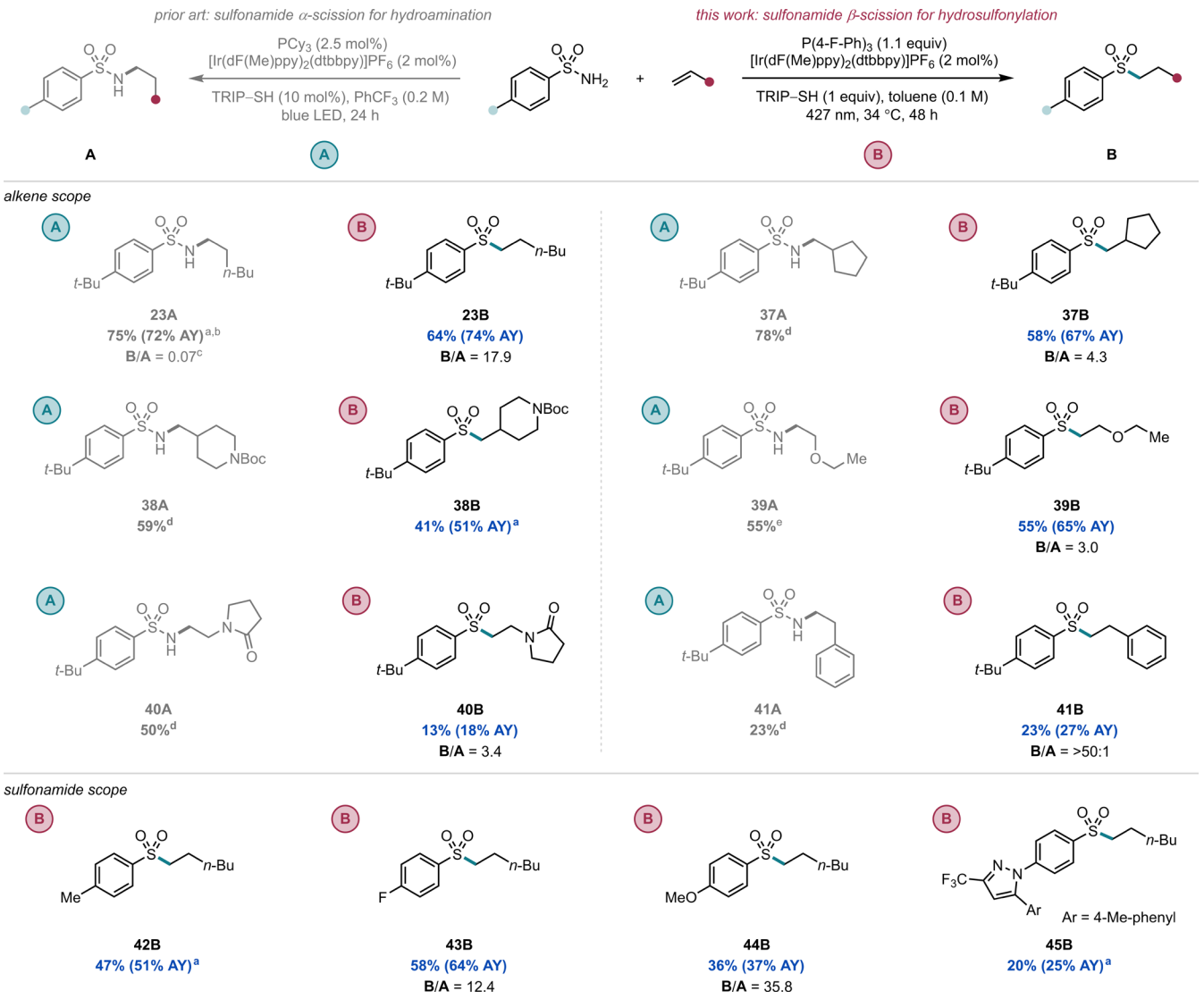

Figure 7. Scope of the developed hydrosulfonylation reaction of primary sulfonamides and comparison to previously reported hydroamination reactions of the same substrates.[29] The results from the hydroamination reaction are reported for 1.0 equiv. sulfonamide and 1.0 equiv. alkene unless otherwise noted.[29] The hydrosulfonylation reaction was performed with 1.0 equiv. alkene and 1.5 equiv. sulfonamide. Yields reported as isolated yield (assay yield). Assay yield determined by GC-FID using 1,3,5-trimethoxybenzene as standard unless otherwise noted. **B**/**A** determined by GC-FID for examples where GC-FID was used to determine assay yield. [a] Assay yield determined by ^{1}H NMR; [b] 5.0 mol % PCy_3, 2.0 equiv. alkene; [c] (**B**/**A**) determined by ^{1}H NMR; [d] Published yields[29] [e] 4.0 mol % PCy_3. **Ir1**, $[Ir(dFMeppy)_2(dtbbpy)]PF_6$; TRIP−SH, 2,4,6-triisopropylbenzenethiol; Boc, *tert*-butoxycarbonyl.

have increased rates of formation for product **A** and decreased **B**:**A** ratios compared to simple unactivated alkenes such as hexene.

Development of a Hydrosulfonylation Reaction from Primary Sulfonamides

With this framework for selectivity outcomes for phosphoranyl-radical-mediated reactions, we aimed to develop a new hydrosulfonylation reaction of alkenes with primary sulfonamides, which would represent the first example of switchable scission reactivity outcomes for a single nucleophile class based on phosphine identity. Using our MLR model, we selected phosphines with high predicted **B**/**A** ratios and screened them under reaction conditions analogous to those used for hydroamination. We found that of the phosphines evaluated, P(4-F-Ph)$_3$ (**P1**) represented the best combination of yield and selectivity; some phosphines that were predicted to be more selective provided no observable yield in this transformation, likely because of increased phosphine oxidation potentials. While this shows that our selectivity prediction model cannot account for reaction yield, it demonstrates how the model can be used to select a targeted screen of phosphines for reaction discovery.

Aiming to develop a method for the selective formation of the hydrosulfonylation product (**B**) for a variety of alkenes, we recognized that we would need to harness both phosphine identity and reaction stoichiometry to achieve **B**-selectivity for more electron-rich alkenes such as **34** and **35**. As such, optimization efforts focused on changing the phosphine and alkene ratio for improved **B**-selectivity. Ultimately, we found that combining the **B**-selective phosphine **P1** with reaction conditions in which the alkene is the limiting reagent led to good yield and excellent **B**:**A** selectivity for our model system, forming **23B** (64% isolated yield, Figure 7). Importantly, the develop-

https://doi.org/10.1021/jacs.6c11233
J. Am. Chem. Soc. XXXX, XXX, XXX−XXX

ment of this transformation under photoredox-mediated conditions enables the direct use of primary sulfonamides for hydrosulfonylation and demonstrates a complementary transformation to the previously reported phosphine-catalyzed hydroamination reaction:[29] divergent reactivity is observed from the same starting materials, dependent on phosphine identity.

With optimized conditions in hand, the hydrosulfonylation reaction was demonstrated for a variety of alkenes and primary sulfonamides (Figure 7). For the alkene scope, products of the new hydrosulfonylation method (**23B**, **37B**−**41B**) were compared to reported products from the corresponding hydroamination method (**23A**, **37A**−**41A**).[29] Comparing the model hydrosulfonylation substrate, **23B**, to its hydroamination counterpart **23A**, it can be seen that divergent reactivity is now accessible with good yields (64% **23B**, 75% **23A**) and high selectivity (17.9:1 **B**:**A** for **23B**; 0.07:1 **B**:**A** for **23A**) in each case. Interestingly, across the scope of alkenes, yields followed similar trends for both products, with **22**, **33**, and **34** being well-performing alkenes in both methods (products **23**, **37**, **39**), and **35** and **36** being lower-yielding alkenes for both products (**40**, **41**). This comparison showcases sulfonamides as the first nucleophile with tunable selectivity in phosphoranyl-radical-mediated reactions.

Among the hydrosulfonylation products, we found that while hexene provides a high **B**:**A** selectivity of 17.9:1 for **23B**, 1,1-disubstituted methylene cyclopropane (product **37B**), ethyl vinyl ether (product **39B**), and vinylpyrrolidone (product **40B**) provide lower **B**:**A** selectivities of 4.3:1, 3.0:1, and 3.4:1, respectively. These results are consistent with our earlier alkene screen; however, the increased selectivity imparted by our carefully optimized conditions allows for isolation of these products in yields of 13−58%. This highlights the importance of understanding the origin of selectivity in these phosphoranyl-radical-mediated processes for the design of improved synthetic methodologies. A 1,1-disubstituted alkene containing a piperidine scaffold was also tolerated in the reaction, providing **38B** in 41% isolated yield, and a conjugated alkene, styrene, provided excellent selectivity of >50:1, albeit with a decreased yield of 23% for product **41B**.

A variety of *para*-substituted sulfonamides were also suitable for this transformation. The model *para-tert*-butylbenzenesulfonamide (forming **23B**) and *para*-fluorobenzenesulfonamide (forming **43B**) provided similar yields (64% and 58%, respectively) and selectivities (17.9:1 and 12.4:1, respectively), aligned with their performance under screening conditions. Product **42B**, arising from *p*-methylbenzenesulfonamide, was formed in a slightly decreased yield of 47%. The more electron-rich *p*-methoxybenzenesulfonamide yielded the hydrosulfonylation product **44B** with excellent selectivity (35.8:1), aligned with the complete selectivity for product **44B** seen under the screening conditions. The lower yield of **44B** is partially attributed to the lack of solubility for this sulfonamide under the reaction conditions. Finally, the small-molecule pain reliever celecoxib was a suitable substrate for this reaction, providing product **45B** in 20% yield, demonstrating the potential of using this transformation for small-molecule drug modification.

CONCLUSIONS

This work reports a comprehensive study of scission selectivity for phosphoranyl radicals with sulfonamide nucleophiles. Experimental, computational, and data-driven study of a photoredox- and phosphine-mediated model reaction reveals the kinetic origin of selectivity under experimental and saturation conditions, demonstrating that a Curtin−Hammett relationship controls selectivity between β-scission and α-scission products. Based on this relationship, we establish how reaction stoichiometry, phosphine stereoelectronic features, and alkene identity control selectivity under experimental conditions, providing essential insights for the development of new phosphoranyl-radical-mediated transformations. Furthermore, we report a practical multivariable linear regression model for predicting phosphines for β-scission or α-scission selective reactions and demonstrate a hydrosulfonylation reaction of primary sulfonamides, making these nucleophiles the first reported to react with phosphine-controlled tunable selectivity.

Overall, this work expands our understanding of phosphoranyl radical scission mechanisms, which we believe will enable further rational design of phosphoranyl-radical-mediated transformations.

ASSOCIATED CONTENT

Supporting Information

The Supporting Information is available free of charge at https://pubs.acs.org/doi/10.1021/jacs.6c11233.

Computed DFT energies (XLSX)

Interactive phosphine selectivity predictions (ZIP)

DFT computed geometries (ZIP)

EDA computed energies (XLSX)

Experimental Selectivity Data (XLSX)

EDA output files (ZIP)

DFT computed geometries for the phosphoranyl radical feature set (ZIP)

Experimental procedures, description of workflow and dataset collection using *Kraken*, description of machine learning procedures and outcomes, computational details, optimization details, characterization data for the hydrosulfonylation reaction (PDF)

AUTHOR INFORMATION

Corresponding Authors

Matthew S. Sigman − *Department of Chemistry, University of Utah, Salt Lake City, Utah 84112, United States;* orcid.org/0000-0002-5746-8830; Email: matt.sigman@utah.edu

Abigail G. Doyle − *Department of Chemistry and Biochemistry, University of California, Los Angeles, California 90095, United States;* orcid.org/0000-0002-6641-0833; Email: abigaildoyle@ucla.edu

Authors

Emily R. Wearing − *Department of Chemistry and Biochemistry, University of California, Los Angeles, California 90095, United States;* orcid.org/0000-0002-7482-3144

Niharika Prakash Kaushik − *Department of Chemistry, University of Utah, Salt Lake City, Utah 84112, United States*

Samuel T. Hugie − *Department of Chemistry and Biochemistry, University of California, Los Angeles, California 90095, United States;* orcid.org/0009-0000-8402-6870

Complete contact information is available at: https://pubs.acs.org/10.1021/jacs.6c11233

Author Contributions

The manuscript was written through contributions of all authors. All authors have given approval to the final version of the manuscript.

Notes

The authors declare no competing financial interest.

■ ACKNOWLEDGMENTS

Financial support was provided by the National Science Foundation Center for Computer Assisted Synthesis (NSF CCAS CHE-2202693) for data science and computational portions of this work and the National Institutes of Health (NIGMS R35 GM126986) for the experimental portions of this work. E.R.W. acknowledges financial support from the National Institutes of Health under the Ruth L. Kirschstein Research Service Award (NRSA) fellowship (F32GM155984). S.T.H. acknowledges the support of the Natural Sciences and Engineering Research Council of Canada (NSERC), [funding reference no. 599238]. For NMR spectroscopy resources, we acknowledge the National Science Foundation grant no. CHE-1048804 and the NIH Office of Infrastructure Programs grant S10OD028644. This work used computational and storage services associated with the Hoffman2 Cluster, which is operated by the UCLA Office of Advanced Research Computing's Research Technology Group. We thank Flora Fan, Alexander J. Maertens, and Dr. Simone Gallarati for helpful discussions regarding this work.

■ REFERENCES

(1) Crespi, S.; Fagnoni, M. Generation of Alkyl Radicals: From the Tyranny of Tin to the Photon Democracy. *Chem. Rev.* **2020**, *120* (17), 9790−9833.

(2) Fagnoni, M.; Ravelli, D.; Protti, S. 2.6 Generation of Carbon-Centered Radicals by Photochemical Methods. In *Free Radicals: Fundamentals and Applications in Organic Synthesis 2*, 1st ed.; Thieme Verlag, 2021 DOI: 10.1055/sos-SD-233-00118.

(3) Shaw, M. H.; Twilton, J.; MacMillan, D. W. C. Photoredox Catalysis in Organic Chemistry. *J. Org. Chem.* **2016**, *81* (16), 6898−6926.

(4) Mitsudo, K.; Suga, S. 2.9 Electrochemical Organic Synthesis via Radical Species. In *Free Radicals: Fundamentals and Applications in Organic Synthesis 2*, 1st ed.; Thieme Verlag, 2021 DOI: 10.1055/sos-SD-233-00170.

(5) Hou, Z.-W.; Xu, H.-C.; Wang, L. Electrochemical Generation and Utilization of Radical Intermediates. *Curr. Opin. Electrochem.* **2024**, *44*, No. 101447.

(6) Zeng, X. The Strategies Towards Electrochemical Generation of Aryl Radicals. *Chem. − Eur. J.* **2024**, *30* (54), No. e202402220.

(7) Yan, M.; Kawamata, Y.; Baran, P. S. Synthetic Organic Electrochemical Methods Since 2000: On the Verge of a Renaissance. *Chem. Rev.* **2017**, *117* (21), 13230−13319.

(8) Kaga, A.; Chiba, S. Engaging Radicals in Transition Metal-Catalyzed Cross-Coupling with Alkyl Electrophiles: Recent Advances. *ACS Catal.* **2017**, *7* (7), 4697−4706.

(9) Lee, W.-C. C.; Zhang, X. P. Metalloradical Catalysis: General Approach for Controlling Reactivity and Selectivity of Homolytic Radical Reactions. *Angew. Chem., Int. Ed.* **2024**, *63* (20), No. e202320243.

(10) Perchyonok, V. T. Radicals and Transition-Metal Catalysis: A Complementary Solution to Increase Reactivity and Selectivity in Organic Chemistry*. In *Streamlining Free Radical Green Chemistry*; Royal Society of Chemistry, 2011; pp 296−308 .

(11) McWhinnie, I. M.; Martin, R. T.; Xie, J.; Chen, R.; Kullmer, C. N. P.; MacMillan, D. W. C. Radical Sorting Catalysis via Bimolecular Homolytic Substitution (SH2): Opportunities for C(Sp3)−C(Sp3) Cross-Coupling Reactions. *J. Am. Chem. Soc.* **2025**, *147* (27), 23351−23366.

(12) Bentrude, W. G. Phosphoranyl Radicals. *Phosphorus Sulfur Relat. Elem.* **1977**, *3* (1), 109−130.

(13) Bentrude, W. G. Phosphoranyl Radicals - Their Structure, Formation, and Reactions. *Acc. Chem. Res.* **1982**, *15* (4), 117−125.

(14) Bentrude, W. G. Free-Radical Reactions of Organophosphorus-(III). In *The Chemistry of Organophosphorus Compounds; PATAI'S Chemistry of Functional Groups*; John Wiley & Sons Ltd, 1990; Vol. *1*, pp 531−566 DOI: 10.1002/9780470034439.ch14.

(15) Leca, D.; Fensterbank, L.; Lacôte, E.; Malacria, M. Recent Advances in the Use of Phosphorus-Centered Radicals in Organic Chemistry. *Chem. Soc. Rev.* **2005**, *34* (10), 858−865.

(16) Rossi-Ashton, J. A.; Clarke, A. K.; Unsworth, W. P.; Taylor, R. J. K. Phosphoranyl Radical Fragmentation Reactions Driven by Photoredox Catalysis. *ACS Catal.* **2020**, *10* (13), 7250−7261.

(17) Pandey, G.; Pooranchand, D.; Bhalerao, U. T. Photoinduced Single Electron Transfer Activation of Organophosphines: Nucleophilic Trapping of Phosphine Radical Cation. *Tetrahedron* **1991**, *47* (9), 1745−1752.

(18) Sinha, P.; Dey, P.; Aneja, Y.; Tilara, A. S.; Dewanji, A. Emergence of Phosphinium Radical Cations as Intermediates for Organic Radical Generation. *Adv. Synth. Catal.* **2026**, *368* (2), No. e70243.

(19) Feng, J.; Nicchio, L.; Liu, L.; Wu, Y.; Lu, K.; Protti, S.; Zhao, X. Recent Advances in Visible Light-Driven Phosphine-Mediated Transformations. *Org. Chem. Front.* **2025**, *12* (5), 1695−1707.

(20) Maddigan-Wyatt, J.; Hooper, J. F. Phosphorus Compounds as Precursors and Catalysts for Radical C−C Bond-Forming Reactions. *Adv. Synth. Catal.* **2021**, *363*, 924−936, DOI: 10.1002/adsc.202001397.

(21) Hu, X.-Q.; Hou, Y.-X.; Liu, Z.-K.; Gao, Y. Recent Advances in Phosphoranyl Radical-Mediated Deoxygenative Functionalisation. *Org. Chem. Front.* **2020**, *7* (16), 2319−2324.

(22) Stache, E. E.; Ertel, A. B.; Rovis, T.; Doyle, A. G. Generation of Phosphoranyl Radicals via Photoredox Catalysis Enables Voltage−Independent Activation of Strong C−O Bonds. *ACS Catal.* **2018**, *8* (12), 11134−11139.

(23) Xie, Z.-Z.; Chen, P.; Huang, C.; Xiang, M.; Gao, J.; Zheng, Y.; Chen, X.-Q.; Chen, K.; Yang, H. Photoredox-Driven Deoxygenative Cross-Coupling of Alcohols with Carbonyl Compounds. *ACS Catal.* **2025**, *15* (24), 20843−20852.

(24) Zhang, M.; Xie, J.; Zhu, C. A General Deoxygenation Approach for Synthesis of Ketones from Aromatic Carboxylic Acids and Alkenes. *Nat. Commun.* **2018**, *9* (1), No. 3517.

(25) Alvarado, J. I. M.; Ertel, A. B.; Stegner, A.; Stache, E. E.; Doyle, A. G. Direct Use of Carboxylic Acids in the Photocatalytic Hydroacylation of Styrenes To Generate Dialkyl Ketones. *Org. Lett.* **2019**, *21* (24), 9940−9944.

(26) Xia, P.-J.; Ye, Z.-P.; Hu, Y.-Z.; Song, D.; Xiang, H.-Y.; Chen, X.-Q.; Yang, H. Photocatalytic, Phosphoranyl Radical-Mediated N−O Cleavage of Strained Cycloketone Oximes. *Org. Lett.* **2019**, *21* (8), 2658−2662.

(27) Han, W.; Liu, W.-D.; Su, J.; Zhao, J. Deoxygenation of Oximes for the Synthesis of Pyrrolines via Hydroimination Cyclization. *Org. Biomol. Chem.* **2023**, *21* (16), 3350−3354.

(28) Clarke, A. K.; Parkin, A.; Taylor, R. J. K.; Unsworth, W. P.; Rossi-Ashton, J. A. Photocatalytic Deoxygenation of Sulfoxides Using Visible Light: Mechanistic Investigations and Synthetic Applications. *ACS Catal.* **2020**, *10* (10), 5814−5820.

(29) Chinn, A. J.; Sedillo, K.; Doyle, A. G. Phosphine/Photoredox Catalyzed Anti-Markovnikov Hydroamination of Olefins with Primary Sulfonamides via α-Scission from Phosphoranyl Radicals. *J. Am. Chem. Soc.* **2021**, *143* (43), 18331−18338.

(30) Kim, J.; Kim, M.; Jeong, J.; Hong, S. Unlocking the Potential of β-Fragmentation of Aminophosphoranyl Radicals for Sulfonyl Radical Reactions. *J. Am. Chem. Soc.* **2023**, *145* (26), 14510−14518.

(31) Zhang, M.; Yuan, X.-A.; Zhu, C.; Xie, J. Deoxygenative Deuteration of Carboxylic Acids with D2O. *Angew. Chem., Int. Ed.* **2019**, *58* (1), 312−316.

(32) Shao, X.; Zheng, Y.; Ramadoss, V.; Tian, L.; Wang, Y. Recent Advances in PIII-Assisted Deoxygenative Reactions under Photochemical or Electrochemical Conditions. *Org. Biomol. Chem.* **2020**, *18* (31), 5994−6005.
(33) Zhang, J.; Mück-Lichtenfeld, C.; Studer, A. Photocatalytic Phosphine-Mediated Water Activation for Radical Hydrogenation. *Nature* **2023**, *619* (7970), 506−513.
(34) Xie, Z.-Z.; Zheng, Y.; Liao, Z.-H.; Yuan, C.-P.; Li, M.-Z.; Deng, K.-Y.; Xiang, H.-Y.; Chen, K.; Yang, H. Photoredox-Catalyzed Hydrogenation of Alkenes Assisted by an in Situ Generated PPh3(OH) Radical and Acetic Acid. *Org. Chem. Front.* **2024**, *11* (15), 4187−4193.
(35) Sedillo, K.; Fan, F.; Knowles, R. R.; Doyle, A. G. Cooperative Phosphine-Photoredox Catalysis Enables N−H Activation of Azoles for Intermolecular Olefin Hydroamination. *J. Am. Chem. Soc.* **2024**, *146* (29), 20349−20356.
(36) Zhu, F.; Qiao, Z.; He, N.; Nong, C.; He, Q.; Xi, M.; Song, X.; Lin, J.; Chen, J.; Jin, Y. Photoredox Catalyzed Hydroazolylation of Alkenes via Phosphoranyl Radicals. *Org. Chem. Front.* **2024**, *11* (10), 2839−2844.
(37) Bentrude, W. G.; Hansen, E. R.; Khan, W. A.; Rogers, P. E. Alpha. vs.. Beta. Scission in Reactions of Alkoxy and Thiyl Radicals with Diethyl Alkylphosphonites. *J. Am. Chem. Soc.* **1972**, *94* (8), 2867−2868.
(38) Davies, A. G.; Dennis, R. W.; Griller, D.; Roberts, B. P. A Kinetic Study of α- and β-Scission of Phosphoranyl Radicals, $R_nP(OR)_{4-n}$. *J. Organomet. Chem.* **1972**, *40* (1), C33−C35.
(39) Bentrude, W. G.; Hansen, E. R.; Khan, W. A.; Min, T. B.; Rogers, P. E. Free-Radical Chemistry of Organophosphorus Compounds. III.. Alpha. vs.. Beta. Scission in Reactions of Alkoxy and Thiyl Radicals with Trivalent Organophosphorus Derivatives. *J. Am. Chem. Soc.* **1973**, *95* (7), 2286−2293.
(40) Davies, A. G.; Dennis, R. W.; Roberts, B. P. Homolytic Organometallic Reactions. Part XII. An Electron Spin Resonance Study of the α-Scission of Alkoxyalkylphosphoranyl Radicals in Solution. *J. Chem. Soc., Perkin Trans. 2* **1974**, *2* (10), 1101−1107.
(41) Bentrude, W. G.; Rogers, P. E. Free-Radical Chemistry of Organophosphorus Compounds. V. Reactions of Thiyl Radicals with Alkylphosphonites. Effects of Activation Energies and A Values on the. Alpha. vs.. Beta. Scission Competition. *J. Am. Chem. Soc.* **1976**, *98* (7), 1674−1677.
(42) Bietti, M.; Calcagni, A.; Salamone, M. The Role of Structural Effects on the Reactions of Alkoxyl Radicals with Trialkyl and Triaryl Phosphites. A Time-Resolved Kinetic Study. *J. Org. Chem.* **2010**, *75* (13), 4514−4520.
(43) Lopp, J.; Schmidt, V. Experimental and Computational Investigations into Trivalent Phosphorous-Mediated Radical Thiol Desulfurization *ChemRxiv* 2021 DOI: 10.26434/chemrxiv-2021-fgq3c.
(44) Xie, Z.-Z.; Liao, Z.-H.; Zheng, Y.; Yuan, C.-P.; Guan, J.-P.; Li, M.-Z.; Deng, K.-Y.; Xiang, H.-Y.; Chen, K.; Yang, H. Photoredox-Catalyzed Selective α-Scission of PR3−OH Radicals to Access Hydroalkylation of Alkenes. *Org. Lett.* **2023**, *25* (50), 9014−9019.
(45) Crawford, J. M.; Kingston, C.; Toste, F. D.; Sigman, M. S. Data Science Meets Physical Organic Chemistry. *Acc. Chem. Res.* **2021**, *54* (16), 3136−3148.
(46) Żurański, A. M.; Alvarado, J. I. M.; Shields, B. J.; Doyle, A. G. Predicting Reaction Yields via Supervised Learning. *Acc. Chem. Res.* **2021**, *54* (8), 1856−1865.
(47) Williams, W. L.; Zeng, L.; Gensch, T.; Sigman, M. S.; Doyle, A. G.; Anslyn, E. V. The Evolution of Data-Driven Modeling in Organic Chemistry. *ACS Cent. Sci.* **2021**, *7* (10), 1622−1637.
(48) Gensch, T.; dos Passos Gomes, G.; Friederich, P.; Peters, E.; Gaudin, T.; Pollice, R.; Jorner, K.; Nigam, A.; Lindner-D'Addario, M.; Sigman, M. S.; Aspuru-Guzik, A. A Comprehensive Discovery Platform for Organophosphorus Ligands for Catalysis. *J. Am. Chem. Soc.* **2022**, *144* (3), 1205−1217.
(49) Seeman, J. I. Effect of Conformational Change on Reactivity in Organic Chemistry. Evaluations, Applications, and Extensions of Curtin-Hammett Winstein-Holness Kinetics. *Chem. Rev.* **1983**, *83* (2), 83−134.
(50) Curtin-Hammett Principle IUPAC. *The IUPAC Compendium of Chemical Terminology*; International Union of Pure and Applied Chemistry, 2025 DOI: 10.1351/goldbook.C01480.
(51) Henstridge, M. C.; Davies, S. G.; Thomson, J. E.; Compton, R. G. Extending the Curtin−Hammett Principle: The Relative Rates of Intramolecular Cyclisation versus Intermolecular Processes. *Tetrahedron Lett.* **2014**, *55* (11), 1886−1889.
(52) Raghavan, P.; Haas, B. C.; Ruos, M. E.; Schleinitz, J.; Doyle, A. G.; Reisman, S. E.; Sigman, M. S.; Coley, C. W. Dataset Design for Building Models of Chemical Reactivity. *ACS Cent. Sci.* **2023**, *9* (12), 2196−2204.
(53) Samha, M. H.; Karas, L. J.; Vogt, D. B.; Odogwu, E. C.; Elward, J.; Crawford, J. M.; Steves, J. E.; Sigman, M. S. Predicting Success in Cu-Catalyzed C−N Coupling Reactions Using Data Science. *Sci. Adv.* **2024**, *10* (3), No. eadn3478.
(54) It is possible that in these systems the more stabilized benzylic radicals formed post NCR-addition can undergo unproductive side reactions such as oligomerization. While we could not identify definitive evidence of these processes, any process which decreases the concentration of alkene in the reaction could influence selectivity through modulation of the phosphine to alkene ratio. For alkenes which can undergo such alternative unproductive processes, selectivity may not follow the expected trends with respect to alkene identity.